

Supplemental Information: Multi-illumination-interfered Neural Holography with Expanded Eyebox

1 Interference Fringe Analysis

In the simulation, it has been observed that the period of fringes resulting from the interference of light sources at varying angles is influenced by the dimensions of SLM pixels. The *pixel rounding* contributes to the emergence of a fringe background in the hologram with a larger period, distinct from the period of fringe interference. Notably, this discrepancy can affect the precision of the experimental results.

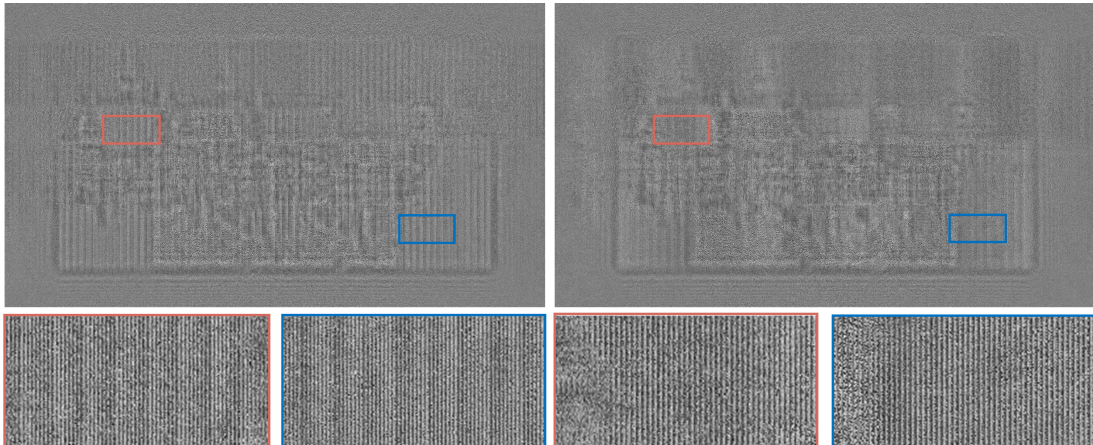


Figure 1: The correlation between the interference fringe period and the SLM pixel pitch for CGH. Left: the fringe period does not align as an integer multiple of the pixel pitch; Right: the fringe period aligns precisely as an integer multiple of the pixel pitch.

Figure 1 presents a hologram generated by horizontally shifting the 3D displacement platform by 4 mm, utilizing a collimating lens with a 300 mm focal length, resulting in an illumination angle of $\pm 0.7639^\circ$ for the light beams. The calculated interference fringe period is $19.9517 \mu\text{m}$, occupying 3.11 SLM pixels. However, a larger-period fringe emerges in the background due to the non-integer multiple of the SLM pixel spacing. This issue can be mitigated by setting the fringe period as an integer multiple of the SLM pixel spacing. In Fig.1, featuring a fringe period of $19.2 \mu\text{m}$ occupying three SLM pixels and an illumination angle of $\pm 0.7964^\circ$, only fringes of the three-pixel period are visible on the background of the hologram. This configuration eliminates the presence of large-period fringes, ensuring the accuracy of the experimental results.

2 Analysis on Energy Efficiency

Energy efficiency is crucial for consumer holographic displays, and our dual-source illumination using a laser beam splitter achieves comparable average power efficiencies of 13.27% (dual-source) against 14.53% (single-source) over the entire supported eyebox. While single-source efficiency peaks at the center viewpoint, it diminishes significantly near the eyebox edges; our dual-source design provides more consistent efficiency across the required field of view without increasing the overall average power.

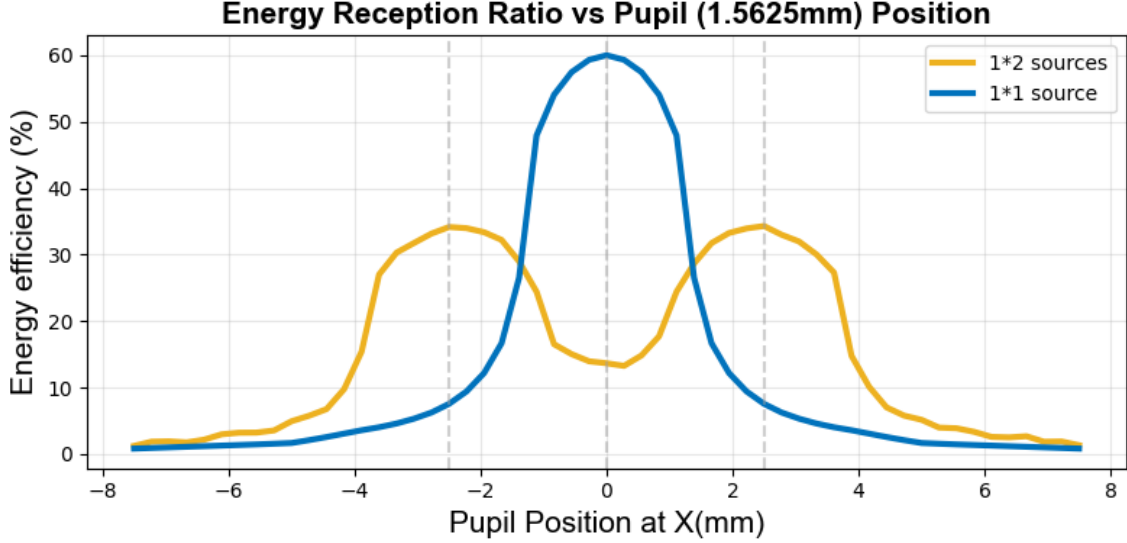


Figure 2: Energy efficiency distribution with pupil position. Simulated comparison of energy efficiency (entering 1.5625 mm pupil) across the expanded eyebox under single-source and dual-source ($\pm 0.7185^\circ$) illumination reveals location-dependent efficiency. The average power efficiencies are 14.53% for single-source and 13.27% for dual-source. While single-source efficiency peaks at the center viewpoint, it diminishes significantly near the eyebox edges; our dual-source design provides more consistent efficiency across the required field of view without increasing the overall average power.

3 Parameters

Concerning the experimental setup, this simulation assesses the influence of varying illumination angles and the number of light sources on a holographic near-eye display operating under multi-angle lighting.

From the simulation results shown in Fig. 3 and Fig. 4, the image quality decreases significantly with increasing number of illuminated lights. This is because aliasing artifacts become more severe as the number of light sources increases, thereby hindering optimization towards the desired image quality. However, the simulation results indicate that even with nine superimposed light sources, the PSNR remains above 25 dB, demonstrating the effectiveness of the proposed algorithm.

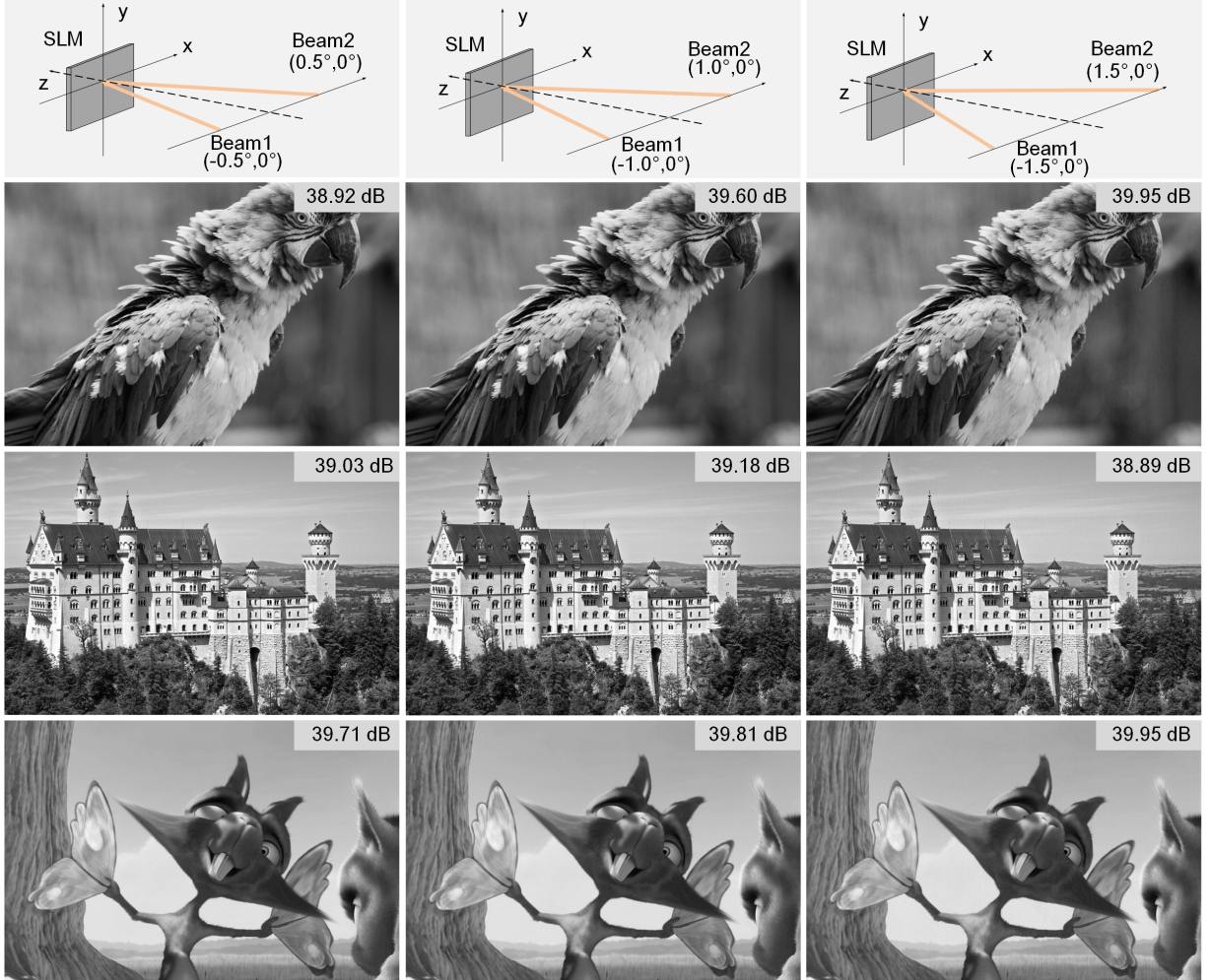


Figure 3: Effect of illumination angle on reconstruction results. The figure illustrates the impact with two beams of illumination light. The first, second, and third columns correspond to light source distributions of $(\pm 0.5^\circ, 0^\circ)$, $(\pm 1.0^\circ, 0^\circ)$, and $(\pm 1.5^\circ, 0^\circ)$, respectively. Despite the increasing angle, the simulation reproduction quality remains unchanged, with all images maintaining good quality. This suggests that the effect of angle change on multi-angle illumination is not significant.

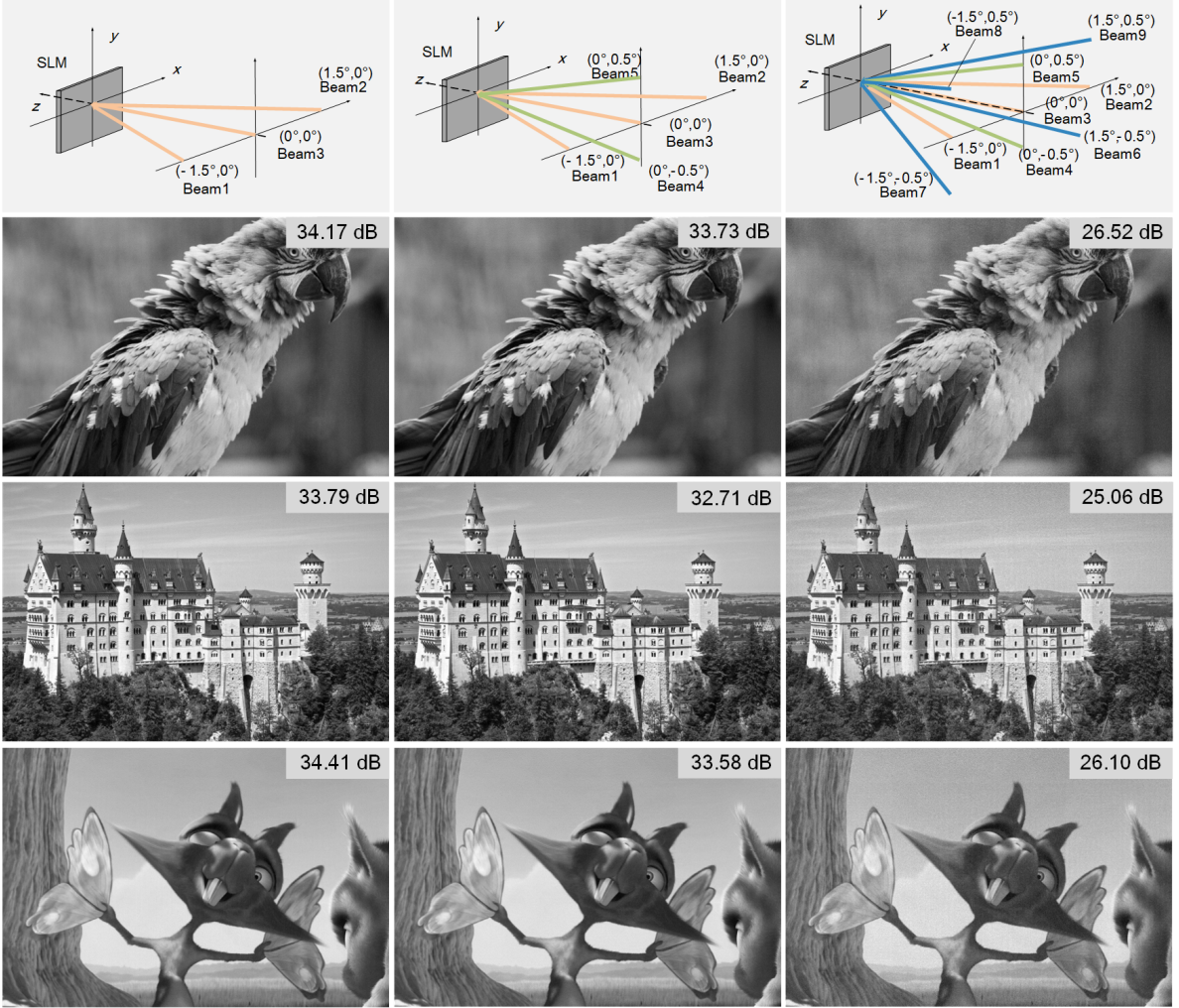


Figure 4: The effect of the number of illuminated lights on reconstruction results. The first column shows the distribution of three light sources, and the three angles correspond to $(\pm 1.5^\circ, 0^\circ)$ as well as $(0^\circ, 0^\circ)$, respectively. The second column shows the distribution of five light sources, and the five angles correspond to $(\pm 1.5^\circ, 0^\circ)$, $(0^\circ, 0^\circ)$, and $(0^\circ, \pm 0.5^\circ)$, respectively. The third column shows the distribution of nine light sources, and the nine angles correspond to $(\pm 1.5^\circ, 0^\circ)$, $(0^\circ, 0^\circ)$, $(0^\circ, \pm 0.5^\circ)$, and $(\pm 1.5^\circ, \pm 0.5^\circ)$, respectively. As the number of illuminating lights increases, the quality of the images decreases instead, suggesting that enforcing more light sources does not always lead to improved results.

4 Additional Simulation Results

Additional simulation results are presented in Fig. 5, Fig. 6, Fig. 7, Fig. 8, Fig. 9 and Fig. 10, which encompasses variations in pupil positions and algorithms for consistent pupil size, as well as changes in pupil sizes and positions with the same algorithm.

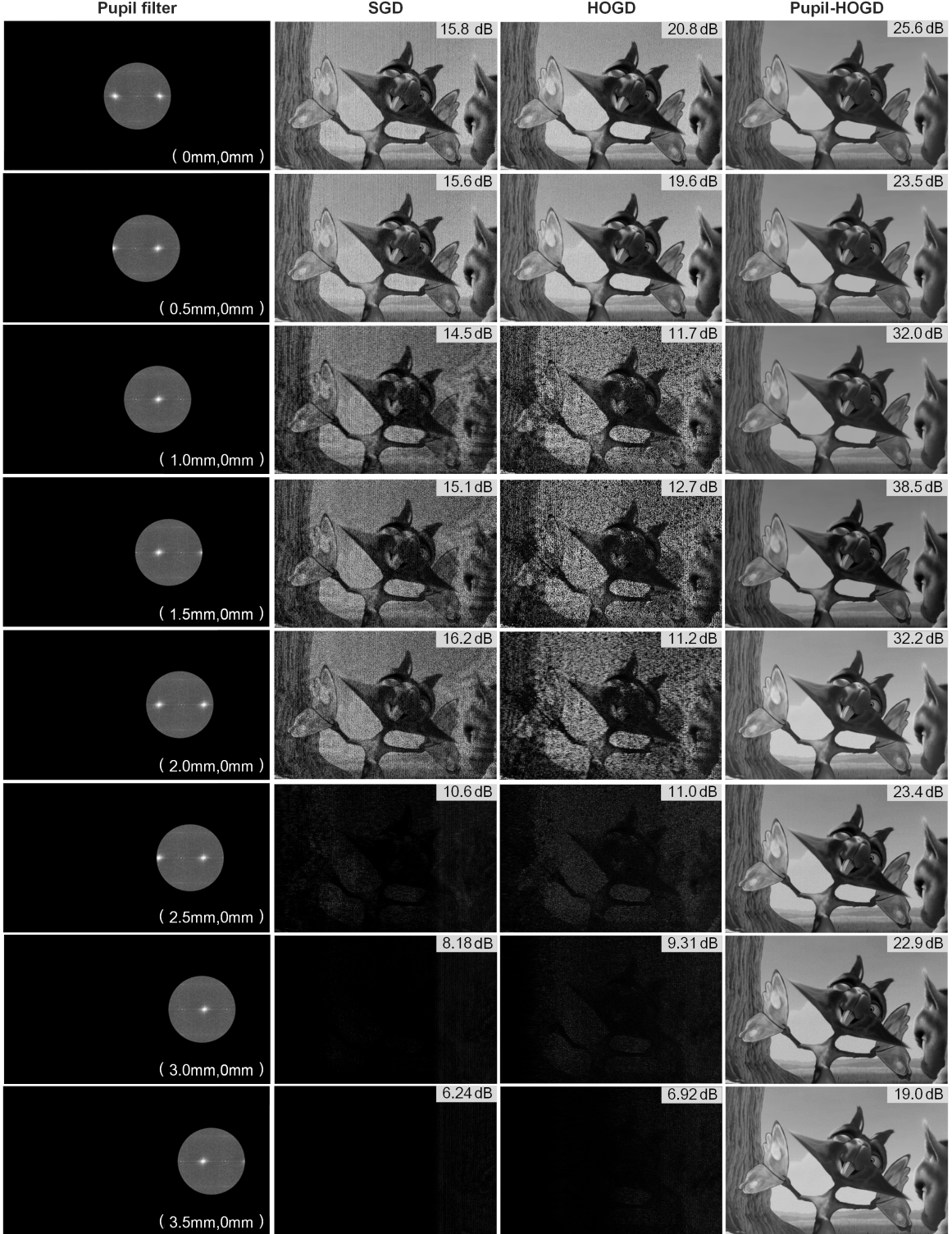


Figure 5: Reconstruction quality of fox images with varying pupil displacements ($D_p=4$ mm). The first column depicts the pupil positions, followed by columns showcasing the reconstructions generated by SGD, HOGD, and Pupil-HOGD algorithms. PSNR values are provided to quantify the performance of each method.

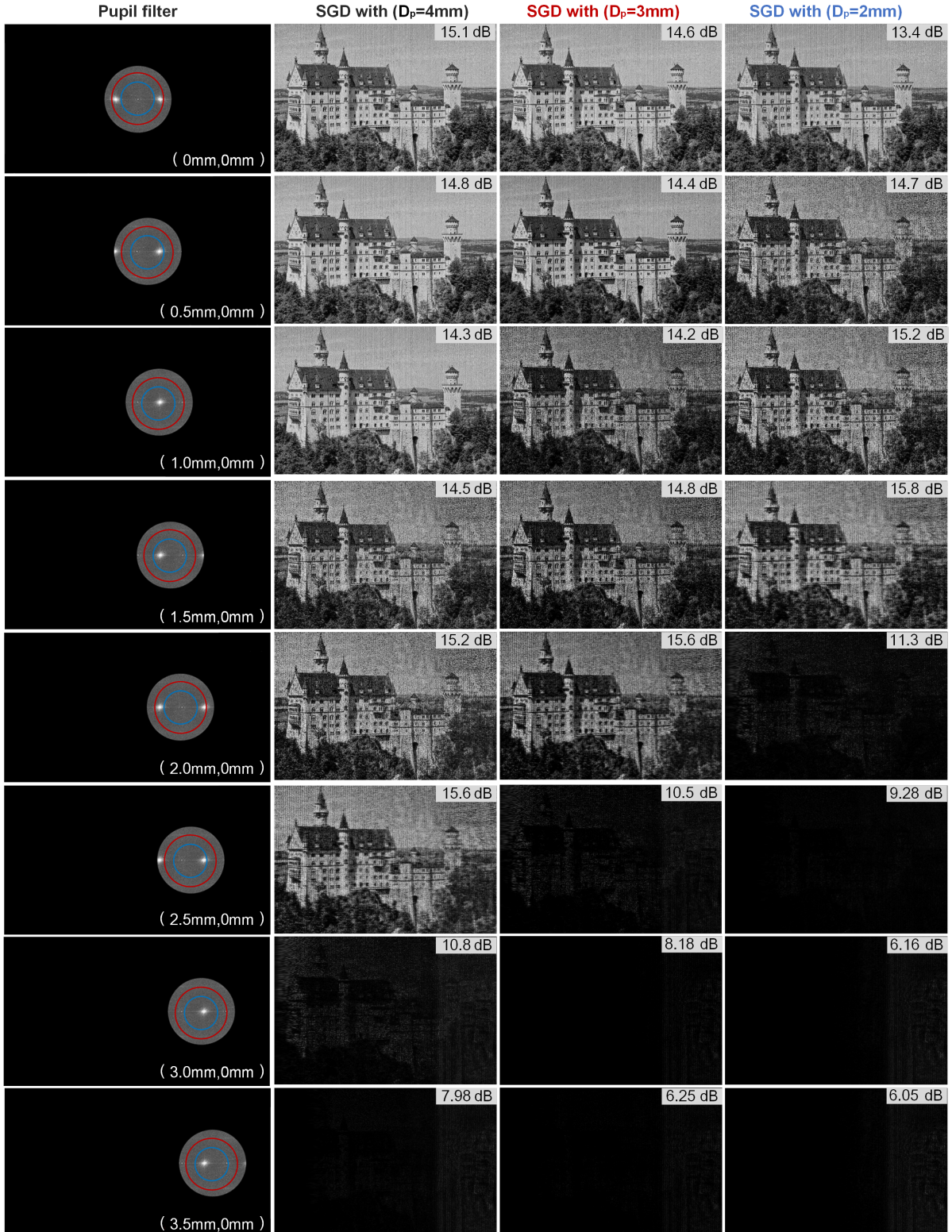


Figure 6: Reconstructed castle images with varying pupil sizes and positions. Pupil positions are illustrated in the 1st column, with subsequent columns showcasing SGD reconstructions with varying pupil sizes. PSNRs are presented to quantify image quality under different conditions. The size of the pupil at 2 mm is indicated by a blue circle, while that at 3 mm by a red circle for clarity.

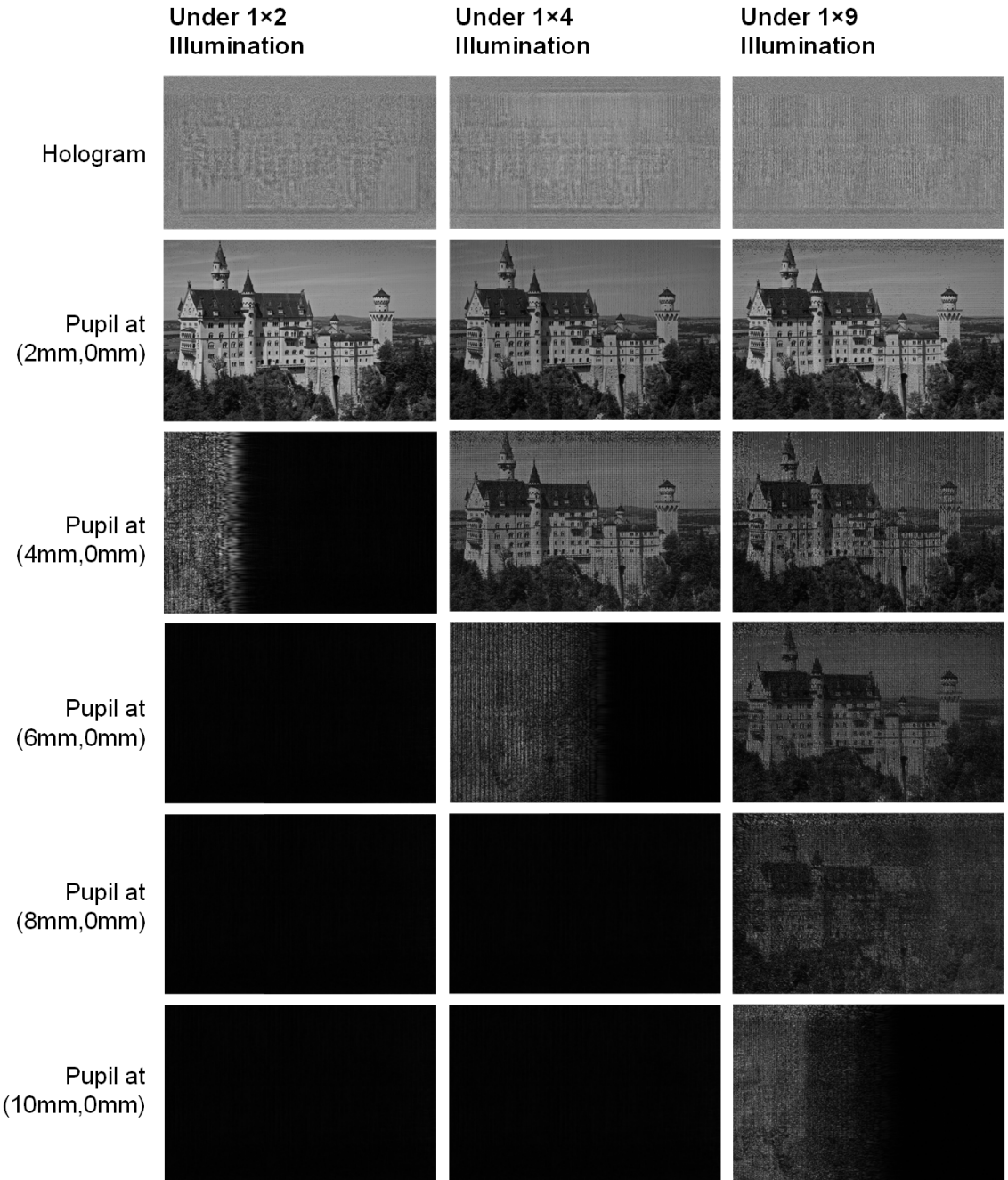


Figure 7: Horizontal eyebox expansion capabilities versus number of illumination sources. Simulated eyebox expansion demonstrates a correlation between source count and viewing area, with a 1×9 configuration achieving $4 \times$ the expansion of 1×2 systems. However, increasing source count introduces progressive image degradation due to coherent interference artifacts. While angular density enhances pupil coverage, practical implementation favors dual-source illumination (1×2) as optimal tradeoff between eyebox gain (50% expansion), system complexity, and minimal quality degradation.

Eyebox Under 1×1 Illumination

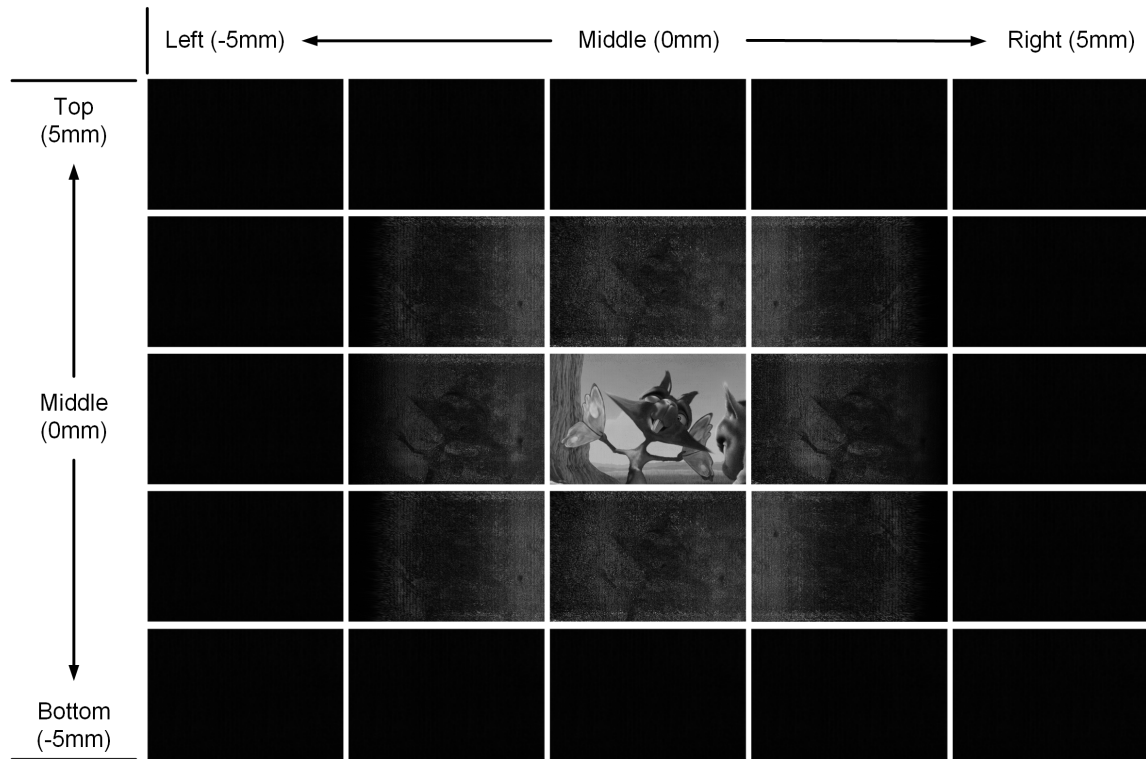


Figure 8: Eyebox under single-source (1×1). This configuration provides optimized central image quality at the viewpoint origin, but confines the artifact-free eyebox to a limited ± 2.0 mm range in both dimensions due to fundamental étendue constraints.

Eyebox Under 2×2 Illumination

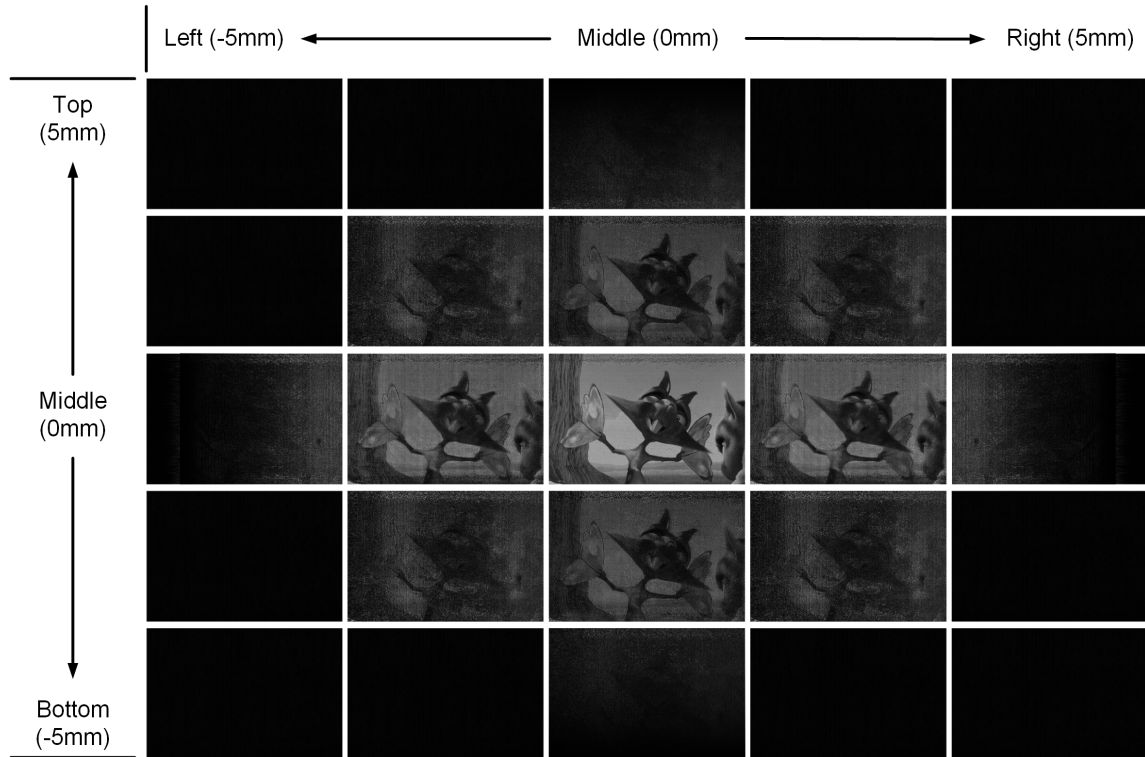


Figure 9: Eyebox under multi-sources (2×2). Extending illumination to four sources with uniform 0.7185° angular spacing achieves $1.5 \times$ area expansion enabling ± 3.5 mm pupil displacement, though introducing moderate central quality reduction due to coherent interference between adjacent viewpoints during simultaneous pupil capture.

Eyebox Under 3×3 Illumination

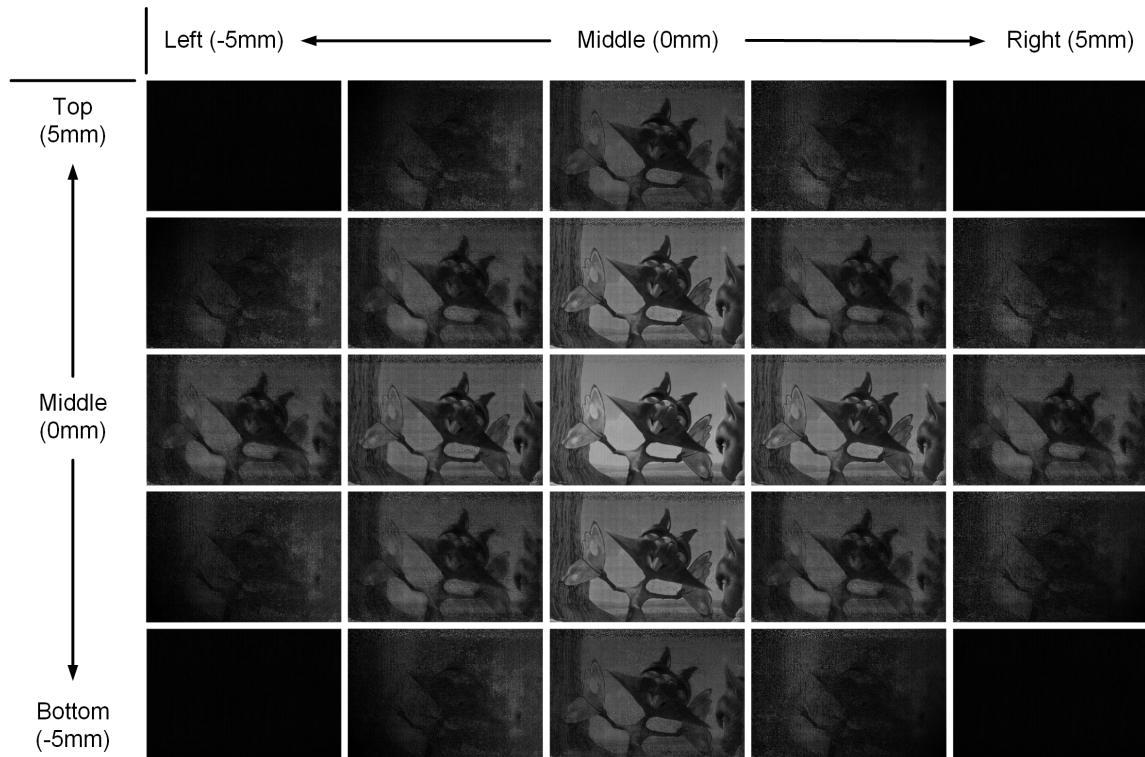


Figure 10: Eyebox under multi-sources (3×3). The nine-source configuration demonstrates $2.25 \times$ linear expansion relative to single-source baselines, supporting ± 4.5 mm omnidirectional pupil movement with maintained peripheral image fidelity, despite progressive center quality compromise from cumulative interference artifacts across the extended angular spectrum.

5 Additional Experimental Results

Additional experimental results are presented in Fig. 11 and Fig. 12 showing the captured results of HOGD, Pupil-HOGD and Pupil-HOGD with CITL under single and dual illumination with varying pupil positions.

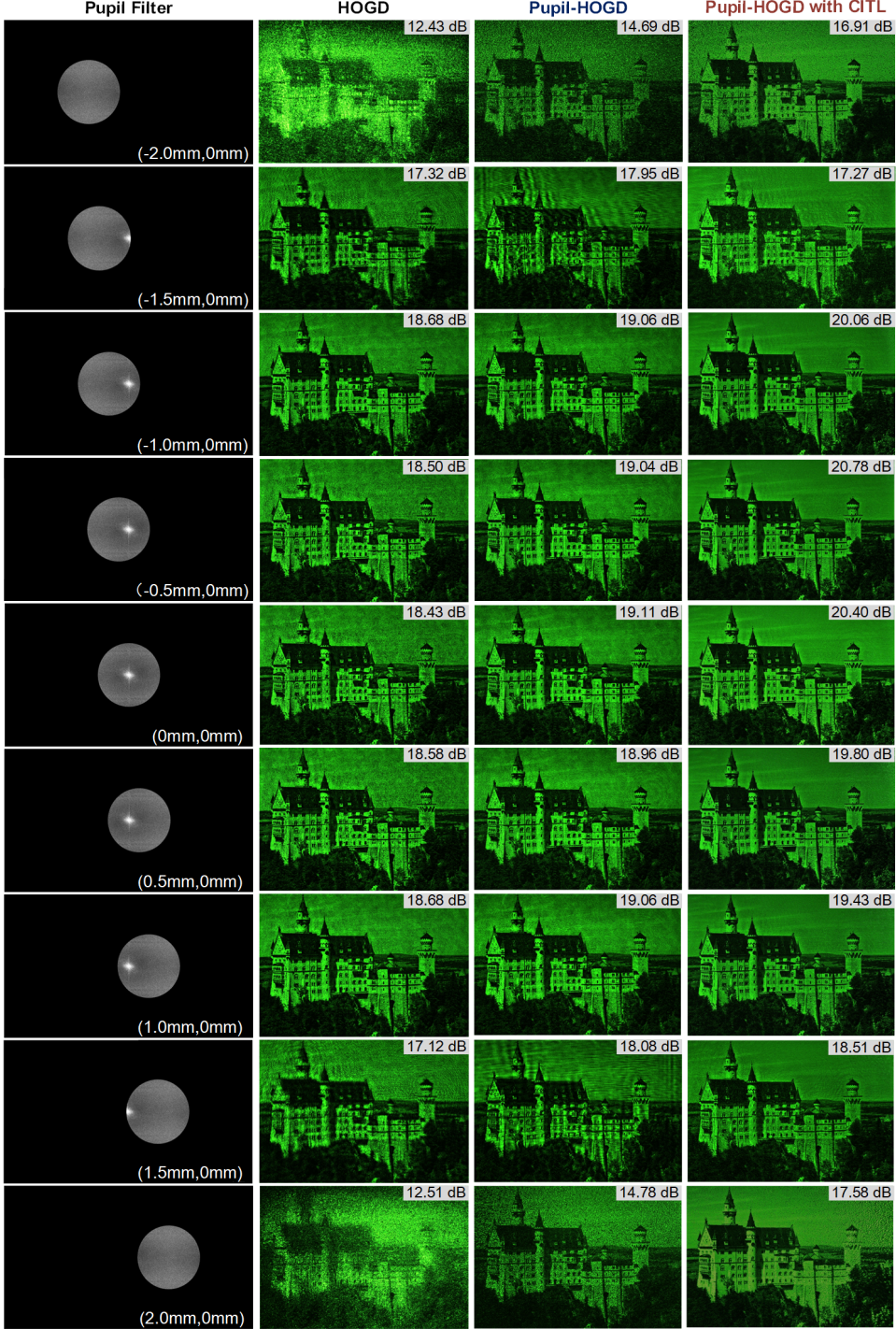


Figure 11: Enhancing image quality in a large pupil near-eye display using the Pupil-HOGD algorithm combined with CITL under single-angle illumination. The experimental results illustrate the improvement across a range of -2.0 mm to 2.0 mm, with 0.5-mm intervals. The optimization effectively resolves image inhomogeneity and background noise, yielding very good image quality up to ± 0.5 mm. Beyond ± 2.0 mm, the pupil shift is too great, resulting in missing images despite advanced subentry techniques.

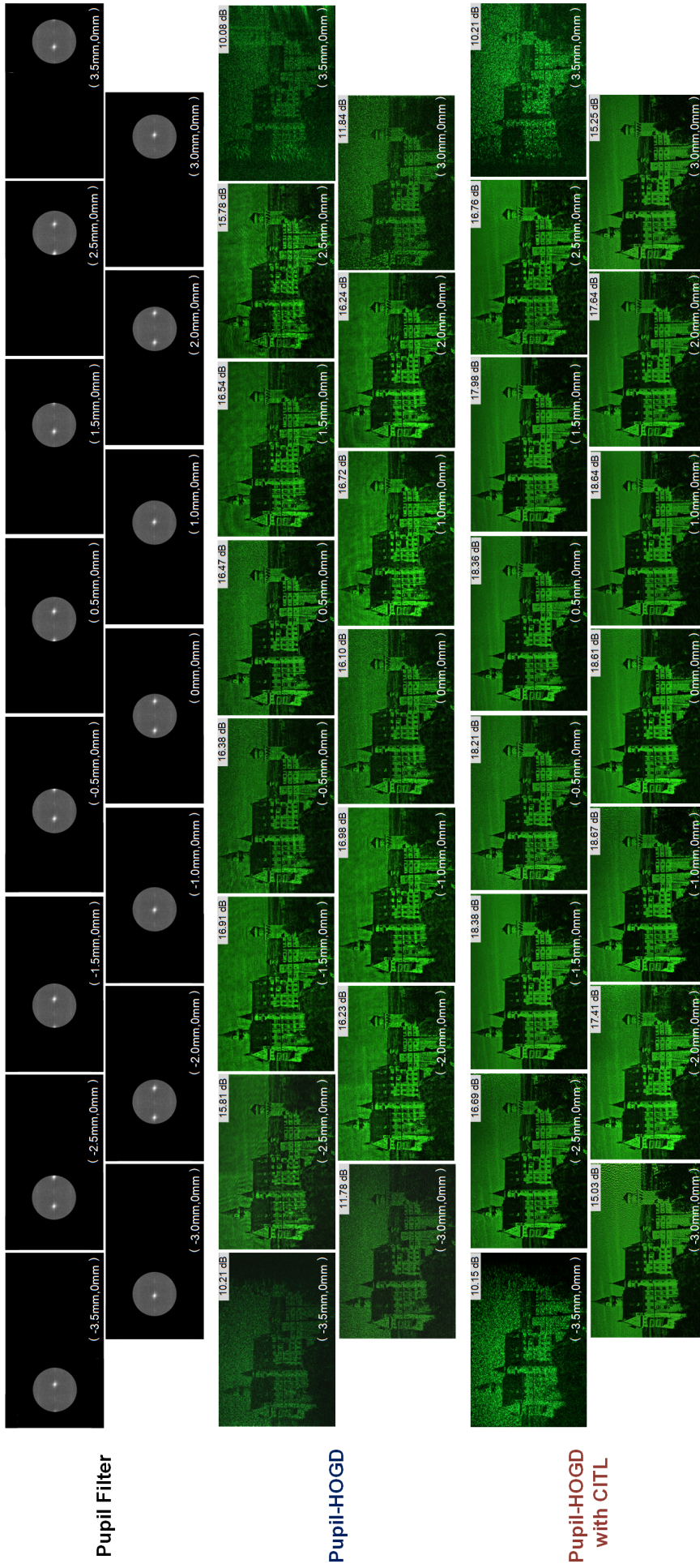


Figure 12: Experimental verification of a large-pupil holographic near-eye display with multi-angle illumination. The display utilizes a pupil diameter of 3.125 mm and illumination light angles of $(\pm 1.2^\circ, 0^\circ)$. The interference fringe period is $12.8 \mu\text{m}$, corresponding to twice the pitch of the SLM pixel. With a propagation distance of 80 mm, the center-to-center distance of two viewpoints is 2 mm, representing a 1 mm expansion of the coaxial basis. The pupil is scanned horizontally from -3.5 mm to 3.5 mm in 0.5 mm intervals.

The integrated multi-angle illumination and Pupil-HOGD optimization enables artifact-free holographic display across a ± 3.0 -mm horizontal eyebox, resolving inherent limitations of scanning-based systems—specifically eliminating temporal bandwidth constraints and image aliasing during pupil movement, through real-time pupil-adaptive CGH synthesis.

6 Towards Compact Implementation

Our bench-top implementation currently addresses the critical challenge of étendue expansion. For eventual holographic displays, additional hurdles including compact form factor must be overcome. While this study does not propose compact solutions, we reference potential pathways toward miniaturization.

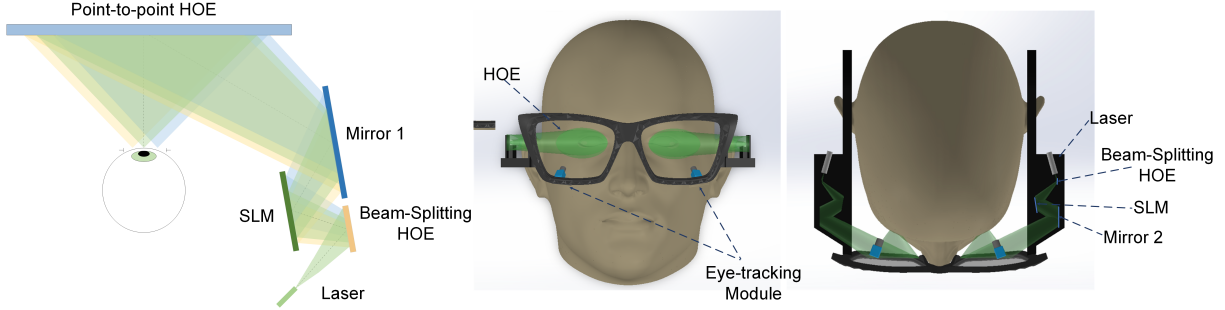


Figure 13: This compact holographic near-eye AR display prototype employs fiber-coupled lasers for multi-source illumination, incorporates beam-folding mirrors and an SLM for phase modulation, and integrates a reflective eyepiece-type point-to-point HOE at the optical terminus to simultaneously converge light rays and fuse real-world scenes with virtual content.

7 Pseudocodes

This section presents the pseudocodes for the proposed algorithms discussed in this paper. Algorithm 1 details the custom hologram generation method. It integrates multi-angle illumination propagation and stochastic gradient descent-based hologram optimization, accounting for pupil constraints and higher diffraction orders. The input includes the target amplitude $a_{\text{tar}}(x, y)$, propagation distance Δz , tilt angles θ_{x_k} , and θ_{y_k} of the beams, as described in the main text. The output is the optimized phase $\varphi(x, y)$ in the SLM plane.

Algorithm 1 Pupil-HOGD propagation under multi-angle illumination

Require: $a_{\text{tar}}(x, y) \in \mathbb{C}^{N \times M}, \Delta z, \theta_{x_k}, \theta_{y_k}$
Ensure: $\varphi(x, y) \in \mathbb{R}^{N \times M}$

- 1: **for** $k \leftarrow 1 \dots N$ **do**
- 2: $U_k(\varphi) \leftarrow \exp\{i\varphi\} \exp\{i\frac{2\pi}{\lambda}(x \sin \theta_{x_k} + y \sin \theta_{y_k})\}$
- 3: **end for**
- 4: $u(\varphi; \Delta z) \leftarrow \sum_{k=1}^N \text{ASM}(U_k(\varphi), \Delta z)$
- 5: $s \leftarrow s_0$
- 6: **for** $i \leftarrow 1 \dots K$ **do**
- 7: $u_{\text{unfilt}}(f_x, f_y; \varphi; \Delta z) \leftarrow \sum_{i,j=-(a-1)/2}^{(a-1)/2} \mathcal{F}\{u(\varphi; \Delta z)\}(f_x + \frac{i}{p}, f_y + \frac{j}{p})$
- 8: $A(f_x, f_y) \leftarrow \text{sinc}(\pi f_x p) \text{sinc}(\pi f_y p) M(f_x, f_y)$
- 9: $u_{\text{tar}}(\varphi; \Delta z) \leftarrow \text{iFFT}\{u_{\text{unfilt}}(f_x, f_y; \varphi; \Delta z) A(f_x, f_y)\}$
- 10: $\mathcal{L} \leftarrow \|s \cdot |u_{\text{tar}}(\varphi; \Delta z)| - a_{\text{tar}}\|_2^2$
- 11: $\{\varphi(x, y), s\} \leftarrow \text{Backpropagation}(\mathcal{L})$
- 12: **end for**
- 13: **return** $\varphi(x, y)$
